Understanding the Nature of Photometric Observations of Geostationary Satellites

Observations of flux variations form distant light sources has long been used to measure physical characteristics of celestial systems. Determining the orbital periods of binary stars, searching for exoplanets and classifying supernovae are all activities that has been facilitated by such measurements. The resulting time series of brightness variations is called a light-curve. However, limited light-curve investigations have been conducted on near earth objects, a subset of which are geostationary satellites. This text outlines the process of acquiring such light curves, and attempts to uncover the capabilities of such an investigation. To this end, a python program was developed to convert raw telescope images to light-curves. This process involves chaining a series of astronomical techniques and algorithms, to produce satellite light-curves.

Investigation into the nature of GEO observations revealed the data to be essentially two dimensional, thus light-curve observations in this space represents a sampling of a light-plane. Setting up a coordinate space of photometric measurements, allows the measuring of certain features by their angular separation. For example, one of the components of the angle between the satellite's attitude and the observer was estimated to be around 5°, in agreement with broadcasting coverage maps published by the satellite operator.

Since the beginning of the space age, the utility and importance of the geostationary earth orbit (GEO) was apparent. It is now considered the most valuable real-estate in space [1], being the most densely populated satellite orbit. It hosts hundreds of satellites with varying purposes ranging from weather forecasting, broadcasting, tele-communication and other services [2]. Note, the word GEO will be used interchangeably in this text to refer to the orbit and objects in this orbit, the context should make it obvious what is meant (e.g. 'There are 2931 GEO's intersecting the GEO').

The geostationary orbit is located approximately 36,000 km above the earth's equator, and it is defined as the circular orbit (i.e. zero eccentricity and zero inclination) at which any orbiting object will have an orbital period equal to one sidereal day. Any satellite set in the GEO will appear stationary in the sky to an observer from Earth's surface, thus

making it ideal for broadcasting to non-tracking radio receivers (satellite dishes). The GEO is a type of geosynchronous orbit (GSO) which include any orbit with an orbital period of one sidereal day (23 hours and 56 minutes) regardless of eccentricity or inclination. Another important orbit is the low earth orbit, (LEO) which includes any orbit with an altitude less than 2000 km. In the 22nd issue of *Classification of Geosynchronous Objects* published by the European Space Agency, the population of objects in the GEO region were studied. 1582 objects were identified to be in the 'GEO Region', only 519 of which are active and controlled [3]. Since the summer of 2017, at least four GEO satellites have experienced malfunctions, two of which breaking into debris [4]. The debris and failed satellites do not stay in their predefined GEO orbit, gravitational perturbations can send these objects into the paths of other satellites causing a cascade of even more debris. Although extensive surveying of debris has been conducted through radio and optical means, limited data is available for smaller debris profile (smaller than 1m) in the GEO [3].

A series of photometric measurements were conducted on a satellite cluster of four satellites, known as the Astra 19.2° E. These satellites provide broadcasting coverage to over 35 countries in Europe, North Africa and the Middle East. Over the course of five nights, more than 5000 images were taken using one of SuperWASP's telescopes out of La Palma.

These images were processed by a custom program that combines a series of astronomical techniques, to produce a total of 20 light-curves. Further processing was done to produce curves with highly legible features.

A limited body of work is available on the subject of GEO light-curves, and no systematic methods for interpreting GEO light-curves was found in the literature. Such as it is, after the results are presented, a framework is developed to set single light-curve data in context with all light-curves available to an Earth-bound observer. This will put certain features in the data-set within a coordinate system that allows for intuitive analysis and interpretation, thus allowing us to assess the efficacy of light-curve observations of GEO objects in the context of other observational methods.

To this end, an overview of the relevant topics in astrodynamics and space science are first covered, followed by a discussion of the astronomical techniques used, how they interlink, and some potential sources of errors and their mitigation techniques. Finally, the results are tabulated and discussed in the context of a accessible photometry space, that produce light-planes instead of light-curves.

I. ASTRODYNAMICS

A. Elliptic Orbits

The most general way to model satellite orbits is with a Keplerian two body system, the orbits follow an elliptical path with the first foci being occupied by the Earth and the second is empty. One can define many useful parameters

2

using this system, such as the inclination i, which is the angle between the equatorial plane and the orbital plane at the ascending node. Eccentricity e given by $e = \sqrt{a^2 - b^2}/a$, is a function of the semi-major axis a and the semi-minor axis b, essentially it tells us how 'squished' the ellipse is, not to be confused with flattening $f = \frac{(a-b)}{a}$ which also describes how 'squished' a reference circle is. The flattening of the Earth is $1/300$, for reference any ellipse with flattening less than $1/50$ is sufficiently small to make it indistinguishable from a perfect circle without precise measurement. The radii of apoapsis r_a and periapsis r_p are the radii of greatest and smallest distance from the earth, see figure 1 for a reference to most elliptic parameters [5].
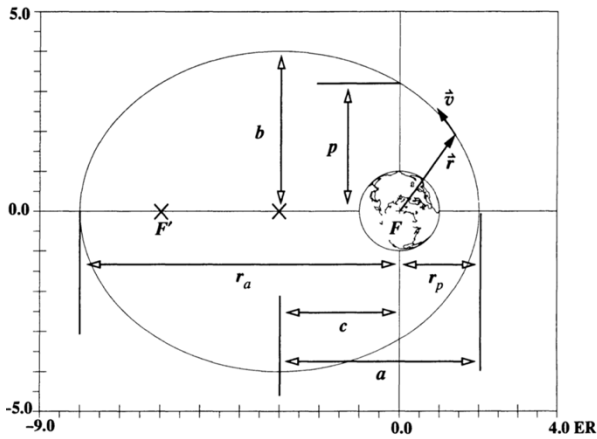
Figure 1. Reference illustration to the main parameters that describe 2D elliptic orbits. Illustration from [5].

There are more orbital parameters needed to completely describe an orbit. However, gravitational perturbations from the Sun, the Moon and mostly Earth (due to its non-uniform mass distribution), cause orbital parameters to constantly drift as a complicated function of all of these forces [6]. For the purposes of orbital path propagation, two-line elements (TLE's) are used, this is a data format used by the US Air Force to publish orbital parameters of known objects [7], this data and the algorithm used to propagate the orbits are publicly available, this method was implemented in later sections to validate positional information and identify satellites by their paths.

B. Geosynchronous Orbits

The geostationary orbit is a subclass of the more general geosynchronous orbit, which is defined as any earth orbit with an orbital period of one sidereal day [6], as such there is an infinite number of possible geosynchronous orbits with varying eccentricities and inclinations. Only one geosynchronous orbit is referred to as geostationary, and it is characterized by a circular orbit (zero eccentricity) and an inclination of $0°$. In practice however, depending on the application, a less restrictive definition is often used. For example, when setting a satellite in the GEO or identifying a GEO object. This is because the GEO is essentially an imaginary circular line that no object can traverse, but with minimal station keeping manoeuvres, a satellite can stay close enough to this line [6].

C. The Population in the GEO

In the 22nd issue of Classification of Geosynchronous Objects published by the European Space Operation Centre, a total of 1582 objects where identified in the 'GEO region', with 512 active and controlled within the GEO, and 795 objects intersecting, or orbiting above or below the GEO [3]. The

ESA's definition of the GEO includes orbiting objects with inclination of up to 25˚, and with the radii $r_a, r_b \in [35586, 35986]$ km.
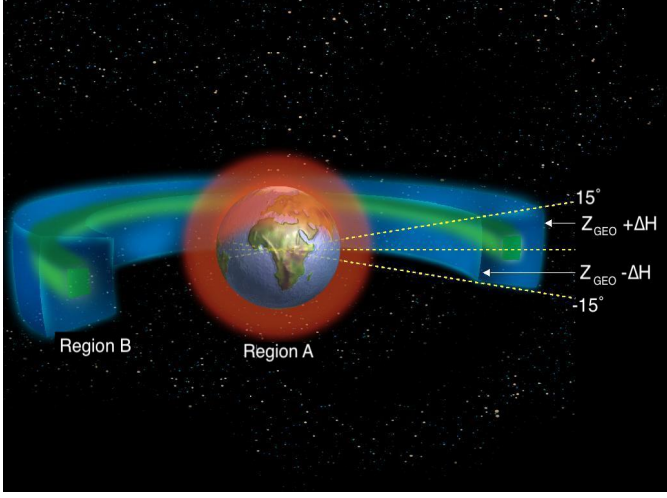
Figure 2. A 3D illustration of the protected regions as set out by the IADC. Region A: low earth protected region, includes any orbit with altitude less than 2000 km. Region B: GEO protected region comprises the toroidal space contained by $i \in [15°, -15°]$ and altitude between the $Z_{GEO} + \Delta H$ and $Z_{GEO} + \Delta H$, with $\Delta H = 200$ km and $Z_{GEO} = 35,786$ km, as defined by IADC in [9].

However, when considering the environment in the GEO, one must also consider objects intersecting the GEO that are not geostationary, the ESA also publishes a yearly environment report accounting for debris in the GEO and LEO, the report identifies a total of 2931 objects in or intersecting the GEO_{IADC} [8], as defined by the Inter-Agency Space Debris Coordination Committee (IADC) [9]. See figure 2 for an illustration of the GEO protected region defined by IADC. Notwithstanding, the detection and tracking limitations of these data sources. As the collated data used by the ESA in their analysis, only include objects that are larger than about 1 m. And only limited surveying of smaller debris have been conducted at geostationary altitudes [10].

D. Coordinate Systems

Geostationary satellites are usually defined by the terrestrial longitude at which they are station kept. For example the four-satellite cluster studied later in this text are called the Astra 19.2˚ E. However, since ground-based optical observations of satellites are taken against the celestial background, it is convenient to track GEOs using a celestial coordinate system. The celestial poles can be defined by extending the Earth's poles, and the celestial plane is defined by extending earth's equator. In celestial coordinates however, Greenwich is no longer the principal longitudinal direction, the Vernal Equinox is used instead, and it is defined by the Sun's ascending node at the intersection between the ecliptic and equatorial plane. Due to the axial precession of the earth with respect to the ecliptic, the Vernal Equinox shifts due west at a rate of 1˚ every 72 years, completing a full rotation in ~26,000 years, because of this, a reference time must also be provided to specify a location in the sky. The common epoch used by astronomers today is J2000 [11].

And instead of longitude and latitude, celestial coordinates use right ascension α and declination δ. Right ascension is usually given in units of **hours minutes second**, because with respect to an earth bound observer the sky is translating at the sidereal rate, making angular measurements along α as easy as counting the time. And the units used for declination is **degrees arcmins arcsecs** [11]. 60 arcmins make a degree and 60 arcsecs make

an arcmin. For an example of using this coordinate system: the location of Sirius is $(\alpha, \delta) = (6h\ 45m\ 8.92s, -16°\ 42'\ 58.08'')$.
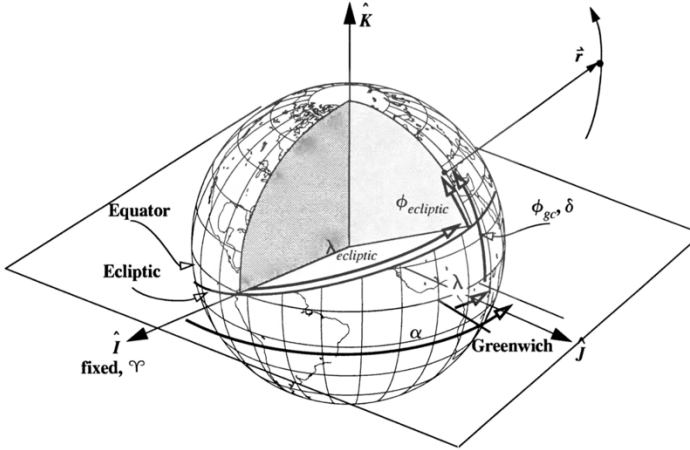
Figure 3. Three different coordinate systems shown: two equatorial systems, terrestrial which uses longitude and latitude (λ, ϕ_{gc}) and celestial which uses right ascension and declination (α, δ); and ecliptic which uses ($\lambda_{ecliptic}, \phi_{ecliptic}$). The principle longitudinal direction for both the ecliptic and the celestial coordinate system is shown by the symbol ♈. Image from [5]

II. ASTRONOMICAL METHODS

For the purposes of GEO satellite observations, many astronomical techniques and methods can be borrowed. Different types of photometric detectors can be used depending on the need, for example a Photomultiplier tubes (PMT) can be used to obtain a high-resolution spectral profile of a light source. Unfortunately, PMTs are essentially a single channel input, so only a single object can be observed at a time [12]. For observations of a large area of the sky, a charged coupled device (or a CCD) is the gold standard, allowing for simultaneous observation of thousands, and sometimes millions of light sources in a single image, e.g. the LSST telescope which has a gargantuan 3.2 gigapixel CCD [13].

A CCD is the silicon chip in the heart of the telescope or camera responsible for collecting the light signal and transforming it into an electrical signal, the CCD chip is divided into a large number of pixels that each count the number of photons incident on them. In other words, a perfect CCD is essentially an array of light buckets that output an $n \times m$ matrix where each element tells us exactly how many photons have been collected [14].

A. Quantum Efficiency

Unfortunately, a CCD is not a perfect array of light buckets, perfect detectors however, are not required for accurate measurements, as long as the electrical signal has a linear response to photon absorption, and photon absorption. CCD's have a finite sensitivity to photons which can be expressed as the ratio of absorbed photons to incident photons, this percentage is known as the Quantum efficiency (or QE) [15]. So, QE is the personage of incident photons that are detected by the CCD, QE is also a function of photon wavelength, so depending on the type of CCD the absorption characteristics will vary, see figure 4 for examples.
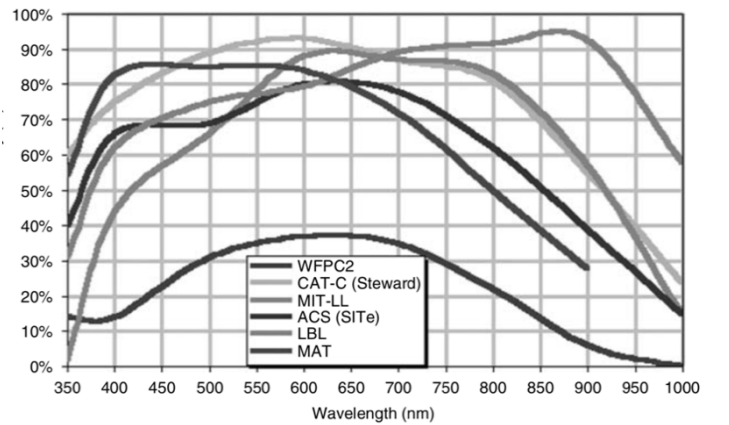
Figure 4. Shows examples of absorption profile of different detectors across the visible spectrum. Figure made by Howell [15].

B. CCD Noise Minimization

Due to the quantum nature of photons, signal to noise characteristics of any photometric detector will obey Poisson statistics, so a count of C will have uncertainty of $C/\sqrt{C}$, this uncertainty is inherent in any photometric measurement [14]. This feature of photometry begs us to increase integration time to maximize our S/N, because as we increase our count by n, the uncertainty increases by $\sqrt{n}$. Unfortunately, as we increase integration time, we risk contaminating our data with spurious detections from cosmic ray. Additionally, CCDs contribute electrical noise, which is also being collected as we increase integration time. Therefore, determining exposure time is an exercise in photon accounting, by maximizing S/N of the object of interest we increase the likelihood of introducing contamination into our data. The sensible approach usually involves acquiring multiple frames, and then median combining, only after applying some sort of outlier removal, that way we get the benefit of a larger S/N without having to worry about spurious data and contaminations.

C. Dark & Bias Subtraction

As mentioned previously, CCDs introduce electrical noise to the data. This noise, however, is somewhat deterministic, which means it can be subtracted from the data frame in the preprocessing stage. Two types of frames are composed to quantify the electrical noise: the Dark frame and the Bias frame. The dark frame is obtained by collecting the 'dark' signal from the CCD while keeping the shutter closed, that way a profile of the dark current can be built up, which is then subtracted from the data frame at the preprocessing stage. The bias frame is similar to the dark frame, where electrical noise is collected for later subtraction, however the integration time is zero [14]. For both bias and dark frame correction, many frames are taken and median combined to get a statistically representative noise profile.
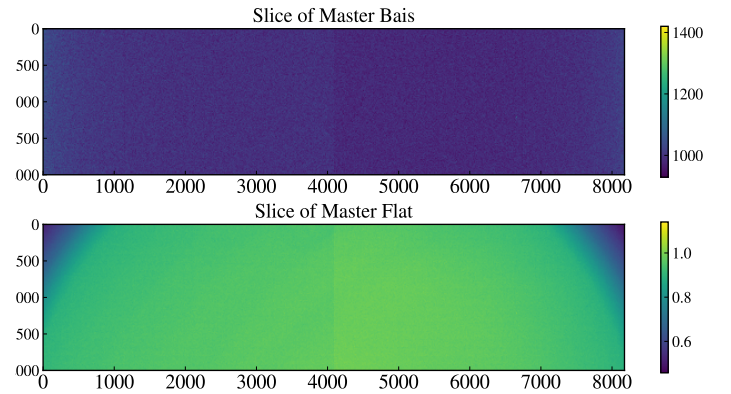
Figure 5. Examples of the reduction frames compiled. The bias frame have an average count of ~ 1000 and shows a gradient of values across the CCD. The twilight flatfield shows the significant nonuniformities due to vignetting, this gets corrected for when dividing the data frame by this frame.

D. Flat-field normalization

All CCDs suffer from nonuniformities, neighboring pixel variations are due to small differences in pixel size, whereas large scale variations are caused by variations in silicon thickness, often a single CCD can be composed of multiple silicon chips which also introduces nonlinearities [14]. In addition, telescope lenses cause a gradient of lower illumination at the edges of the frame, this is known as vignetting and can be seen in the flat frame shown in figure 5. The basic idea of flat-fielding is to expose the CCD to uniform light, integrate, now any variations in detected light

is due to CCD nonuniformities. After normalizing the flat frame, it can now be used to scale the data frame, dividing the data frame by the normalized flat field results in a reduced data frame that can now be used to do science. Looking at figure 4, it is easy to see why the process of flat fielding is not so straight forward, variations QE requires us to flat field with a uniform light that matches the spectral profile of the object of study, this is why many astronomers prefer to take the flat field frame of the twilight sky because it's wavelength spectrum is 'close enough' to celestial objects [15]. For the proposes of this project twilight flats are appropriate, because we are only interested in photometric data from stars and satellites that reflect practically the same 'kind' of light that the twilight sky is reflecting.

E. Astrometry

After all the data frames have been bias subtracted and flat-field normalized, the frame is ready for photometric measurements to be taken. However, for later magnitude calibration and satellite identification, the frame is processed with an astrometric solver, which essentially maps (x, y) coordinates on the frame to celestial coordinates, i.e. $(x, y) \rightarrow (\alpha, \delta)$ [15]. The process involves first extracting (x, y) positions of the stars in the frame and handing it to an algorithm that searches the entire sky for similarly spaced away stars, for a reasonable search time one can limit the search space by restricting allowed (α, δ). The searching algorithm that was used for this project was provided by

astrometry-net, a C based software project, that provides a fast and robust astrometric solver, see D. Lang, et al. for more details [16].

F. Satellite Identification

Satellites and debris in orbit are tracked and monitored by organizations like NORAD and NASA the orbital elements are publicly available and published in the form of TLE's. These TLEs can be used to propagate the position vector forward in time. After obtaining the celestial coordinates of the satellites in the data through the previous step, the celestial paths the satellite takes across the sky can be compared with TLE data to confirm an object's type, origin or id.

Unfortunately, TLE data are only accurate within a radius of about 1 km for active satellites [17], thus for a crowded orbit like the GEO it is often not enough to take a single measurement to identify the object's origin. However by plotting the paths in celestial coordinates it is easy to identify the target object, as will be seen in the results section.

G. Photometry

Time series analysis of flux coming from a celestial body is often used to classify and study celestial sources. Building such a time series (light-curve) involves taking multiple flux measurements from a source over the course of a night, for slowly changing sources such as stars it would be stuffiest to take a single measurement each day, or each month to build up the light-curve. The most commonly used method of obtaining a photometric measurement is to fit a 2D *point*

spread function (PSF) to the source, since almost all astronomical sources can be approximated to a PSF [15].

Another method used is digital aperture photometry, which relies on determining a boundary for the object of interest, typically a circle, and summing pixel values inside the boundary. A thorough review of CCD aperture photometry is outlined by Mighell in [18], a brief description of these steps are discussed here:

1) The first step involved in aperture photometry is obtaining center positions of the object of interest. This can be done using one the standard libraries developed for this, Source Extractor [19] was the package used for this task.

2) A radius r for the object must then be chosen, whose circle contains the object. Typically, $r = FWHM$ (Full Width of Half Maximum) results in best S/N [15].

3) Simple summing of pixels within object aperture gives the total counts of the source, in addition to sky background signal. The sky background can be estimated by summing and normalizing the annulus around the object aperture.

4) Finally, determination of the intensity I can be achieved using aperture flux S_A, estimated background $\bar{B}$, aperture area, here where n_{pix} is number of pixels in the aperture and exposure time t_{exp}, so:

$$I = \frac{S_A - n_{pix}\bar{B}}{t_{exp}} \qquad (1)$$

Now the instrumental magnitude m_I can be determined using the equation [18]:

$$m_I = -2.5 \log_{10}(I) \qquad (2)$$
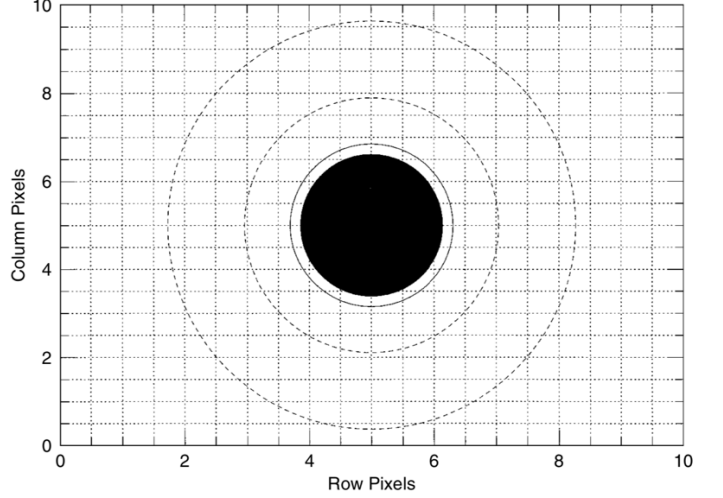
Figure 6. Sketch of a potential star in a CCD frame surrounded by the aperture (solid line) as well as the annulus from which the background is estimated. Diagram from [15].

H. Magnitude Calibration

The magnitude of the object obtained in equation 2 is sufficient for comparing results from the same instrument, however to make comparisons with published findings, each CCD image must be calibrated by a constant called the zero point. The zero point correction allows us to bring our measurements to a standard scale as well as correct for atmospheric extinction [20]. Because the perturbing effects of the atmosphere and the clouds are constantly changing each CCD image must be corrected individually.

The process of obtaining the zero point involves a few steps: First, using the coordinates solved in section II.E one can compile a list of stars with known apparent magnitudes in that slice of the sky. By querying one of the publicly available catalogs

such a list is easy to compile. The catalog used in this project was GAIA 1DR [21] which provides a public API which can easily be interfaced with in python.

Second, identify appropriate star candidates in the CCD image, and using their (α, δ) positions obtained in section II.E, to match stars from the catalog to stars from the data. If the stars have been matched up correctly then the zero point can be read off the table since it's simply the difference between the apparent magnitude from GAIA 1DR and Instrumental magnitude from the data.

The calibrated magnitude m_{calib} can be expressed in terms of the instrumental magnitude m_I and the zero point Z as [20]:

$$m_{calib} = m_I + Z$$

Thus the best value for Z can be found through linear regression. By fixing the m_I coefficient at one our best value for Z becomes the x intersect at $m_{calib} = 0$. To catch miss-matched stars any data point with error above 3 sigma's was discarded.

I. Photometry. What can go wrong?

Typically when taking standard photometric measurements, there are two main sources contamination, incorrect background estimation and source blending. Ground based observations unavoidably suffer from access signal reflected by the sky from various sources, the sun, the moon, and artificial light from cities. Consequently, astronomers have developed sophisticated algorithms to subtract this signal which can appears as a gradient across an image for observations too close to

the moon or observations taken at twiglet. This effect appears in the data and is usually the dominant source of error as we come close to dawn. The choice of algorithm depends on the type of observations made, Source Extractor offers robust routines for background estimation, these were used to subtract the background from the data images, thus discounting the need for separate background estimation for each photometric measurement. Details of the algorithm can be found in [19].
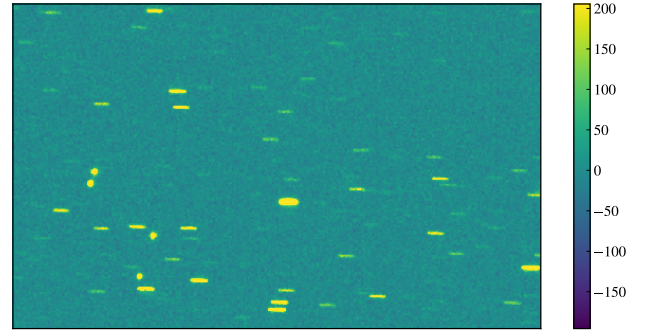
Figure 7. A slice from a reduced CCD image, illustrating the different shapes of stars (horizontal streaks) and satellites (uniform circles) in the data.

Source blending adds additional complication, especially when observing GEO satellites, as the blending is constantly changing as the stellar background is drifting along at the sidereal rate (15°/ hour). Fortunately, the drift rate ensures that contamination from any particular star only appears in one image, say if the CCD is taking 60 images per hour, that is an angular difference of 0.25° per image, thus it will not contribute to the light-curve shape, for reference the angular diameter of the moon as seen from earth is about 0.5°.

Three options are available when taking photometric measurements of GEO objects. The simplest method (and the method used in this project) is to fix the telescope at the desired

coordinate, and since GEOs don't move with respect to a ground observer, no tracking is needed. This can be set up very easily by relatively inexpensive astronomical instruments. However, by looking at figure 7 it is easy to identify a potential source of error, the stars in the data frame appear as streaks and the satellites are point sources. Undoubtedly, this contributes a small discrepancy between the recorded magnitudes of the stellar and the GEO sources. Thus, the zero-point calibration from II.H will potentially be offset from the true zero point of the satellites. If extremely accurate photometric measurements are required, then tracking the sky at half the sidereal rate will produce equally stretched streaks for both the stars and the satellites making photometric measurements more comparable, however for the purposes of this project this is not required, plus this method makes it more difficult to distinguish between stars and the GEO targets. The last option is to track the sky at the sidereal rate, this can be useful for observing LEO objects, which fly across at incredible speeds, too fast for sensible

tracking and by keeping the stars as points the area of potential blending is minimized.

III. RESULTS

The results presented in this text were obtained from over 5000 CCD images taken by one of SuperWasp's CCD arrays. The size of the data necessitated the developing of a light curve extraction program that automates this process. The program structure is essentially a data flow model that pipes the raw images through the various methods and algorithms outlines in section II. The output from processing these images was the twenty light-curves shown in figure 8, the temporal resolution of these light-curves was around 2 brightness readings per minute.

Two of the satellites in focus were designed by Lockheed Martin the 1KR and the 1L, and were launched 2006 and 2007. The other two are a more recent model designed by Airbus Defense & Space, and are based on the Eurostar E3000 platform see table 1 for details on the dimensions and mass.

TABLE I. Details and physical dimensions of the of the four satellites whose light-curves were recorded.

| Name	Manufacturer	Model	Launch date	Mass	Dimensions (H × L × W)	Solar array span	deployable antennas
1KR	Lockheed Martin	A2100	20-04-2006	4332 kg	~3.7 × 1.8 m	-	-
1L	Lockheed Martin	A2100	04-05-2007	4497 kg	~3.7 × 1.8 m	-	-
1M	Airbus D&S	Eurostar E3000	05-11-2008	5320 kg	4 × 2.4 × 2.9 m	35 m	Two 2.4 m One 2.2 m
1N	Airbus D&S	Eurostar E3000	06-08-2011	5350kg	~4 × 2.4 × 2.9 m	35 m	Three 2.6 m. One 1.3 m top-floor steerable.
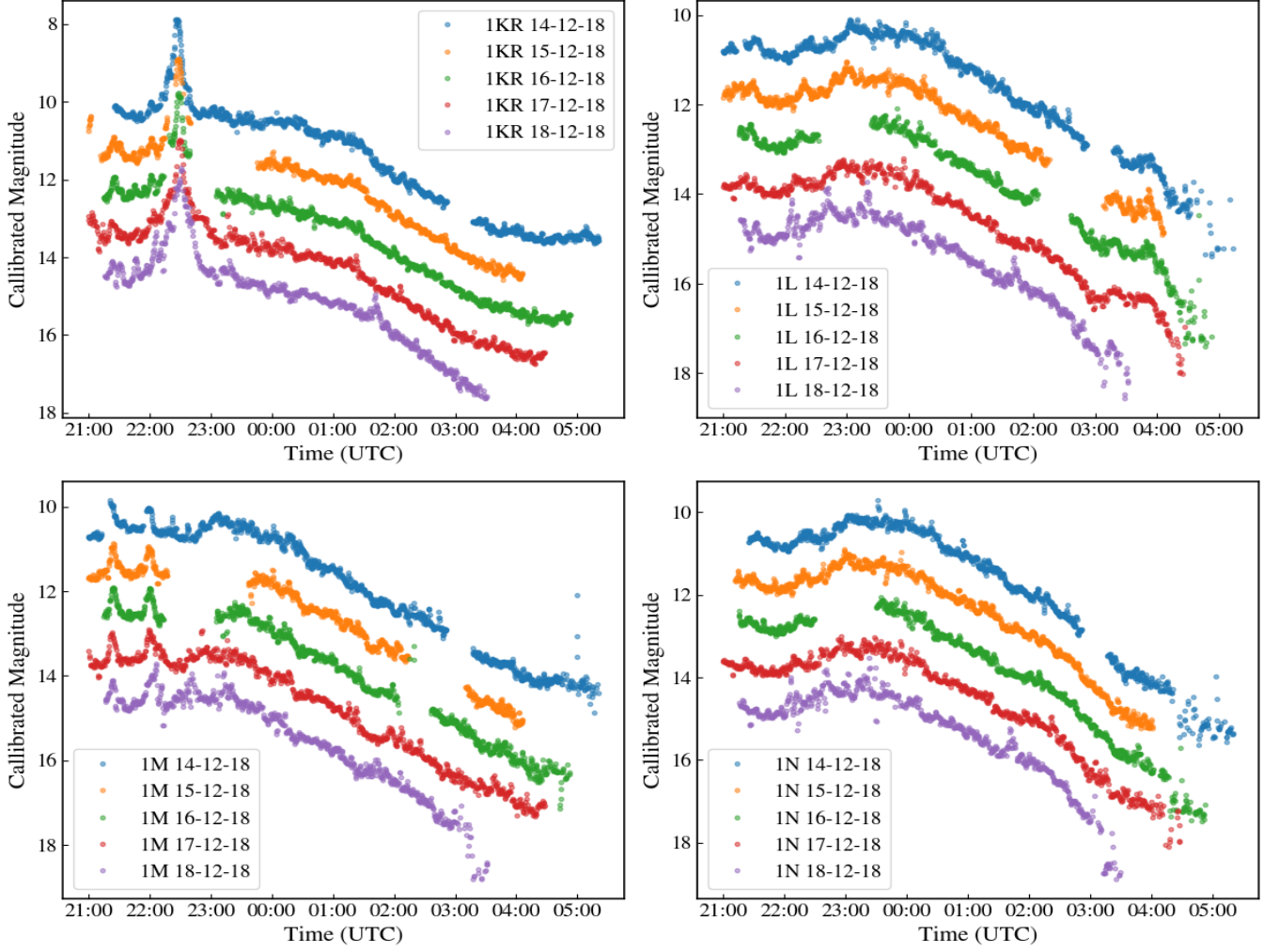
Figure 8. Calibrated light-curves from the four satellites, the curves were offset by +1 magnitude per night so they don't overlap, therefore the curves with the real magnitude in the data are the ones labeled 14-12-18. The gaps in the data are a result contamination from intersecting flight paths, as seen in figure 10 there are at least 3 points were one of the sources is at least partially obscured by another, the instances at which two satellites were detected as one were discarded.
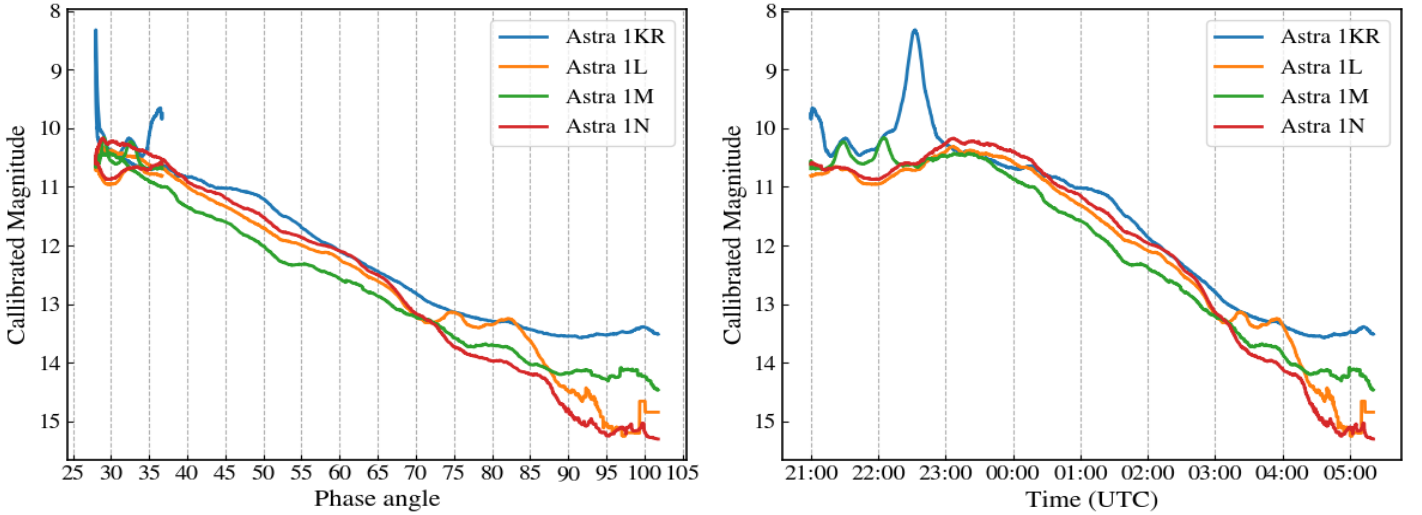

Figure 9. (left) Light-curves plotted against phase angle. Note that features closer to the minimum phase are compressed with respect to features on the right. (right) The light-curves observations against time.
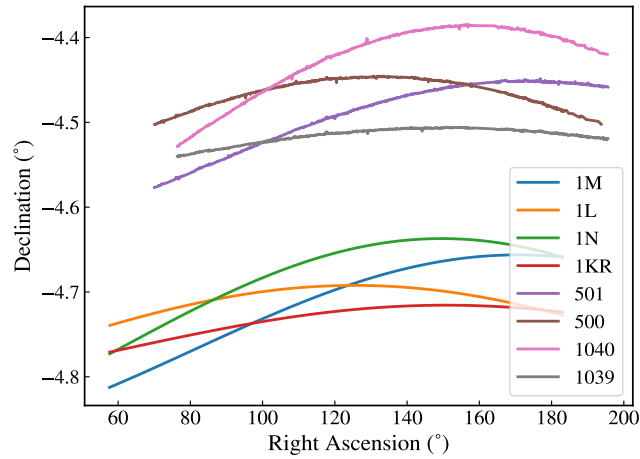
Figure 10. comparison between orbital paths obtained from the CCD measurements and the paths obtained by propagating TLE data between 9:00 pm 14/12/2018 and 5:00 am 15/12/2018 (UTC). By visual inspection it is easy to match the smooth labeled curves to the correct curves from the data. The discrepancy in the positions is a limitation of the TLE data, which has an accuracy window of about 1km for GEO satellites .
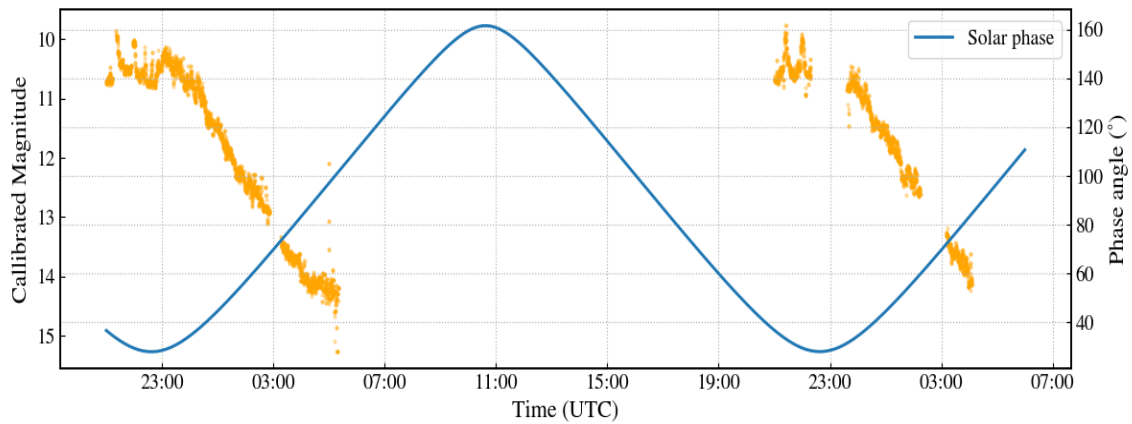
Figure 11. Astra 1M light curves plotted along with the corresponding phase angle.
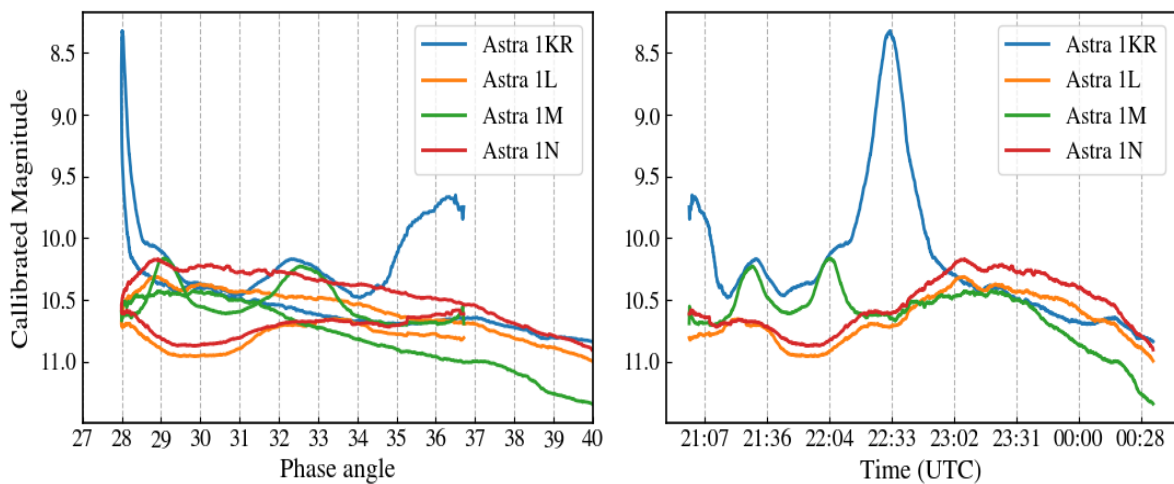
Figure 12. (left) Apparent magnitude of the satellites from the start of the observation run at ~37° it reaches a minimum at 28° which corresponds to a peak the brightness of 1KR. (right) The same data plotted against time.

To access whether the satellites from the same manufacturer show similar features in the light-curves, the satellites were identified using the method outlined in section II.F. The measured orbital paths of the Astra satellites were tabulated and plotted in figure 10 along with propagated paths from TLEs, it is clear by visual inspection which satellite is which.

Notably, no light-curve correlation was found between satellites of the same model.

A. The Astra light-curves

After preprocessing the data in the manner described in section II, light-curves were grouped based on their ids. The light-curves were then drawn with an offset of +1 magnitude per night to illustrate the unchanging nature of the curves from night to night, see figure 8. The gaps in the data are a result of areas of intersection between the satellites, this can be seen in figure 10, were a single detection might include light from more than one satellite, these data were identified and cleaned out.

B. Phase dependent curves

The phase angle φ of an orbiting object is the angular difference between the object-sun vector and the object-observer vector. Since the position vector of the satellite is known in our data, ephemeris of the sun and the earth can be used to calculate the angular difference between the observer and the sun with respect to the satellite. Figure 11 shows the general trend of maximum brightness at minimum phase angle and that the brightness decreases as φ gets larger.

Observing that the light-curves barely changes over the span of the five nights the curves from each satellite were combined for further reduction in noise, the result of this was the highly legible curves shown figures 9.

To achieve this, a few time series smoothing techniques were applied to the data, simply the curves were resampled such that their time indices aligned, then they were median combined, finally a windowed rolling mean of five minutes were applied, the results of which was the curves on the right side of figures 9. This smoothed time dependent curve was used to construct the phase angle dependent curves on the left side of figure 9.

IV. DISCUSSION

The general trend observed with respect to the phase angle is an inverse relationship with brightness, this is exactly what is expected for most shapes. However, many notable features are observed in the data, notably the distinct peek at minimum phase angle by the 1KR satellite, and maximum brightness of the other three occur slightly after the angle of minimum phase. Additionally, the distinct double peak in the 1M curve between phase angles 29° and 32.5°, which overlaps with a similar but less visible feature in 1KR, 1L also shows a similar feature between 75° and 82°. In figure 9 both 1M and 1L double peaks are spaced apart by 30 minutes which might suggest that they arise from the same physical effects, but looking at the left side of figure 9 we see that the phase difference in the 1M and 1KR peaks is 3.5° and for the 1L peaks its 7°. Furthermore the

13

magnitude of 1KR dips until it reaches 90˚, at which point it starts increasing again. Before attempting to interpret these featured some discussion of the geometric and physical nature of the data is due.

A. The geometry of the data

Why is there a phase angle minimum, and why is it 28°? The solar season determine the minimum φ from an observer at the equator. This value oscillates between -23.5˚ and 23.5˚ as we go between the solstices, only at the equinox does a straight line pass through the sun, the equatorial observer and the GEO satellite. The minimum phase angle observed each night represents the moment when the satellite and the observer are in the plane perpendicular to the ecliptic plane (earth's orbital plane around the sun). Thus at the winter solstice, right around the time the data was collected, the expected minimum phase angle for an equatorial observer is around 23.5˚, the telescope used for this experiment is located 28˚ north from the equator which after some approximate trigonometric calculations is found to add an additional ~4.5˚ to the minimum phase angle.

B. From Light-curve to Light-plane

When examining a set of data, it is often instructive to look at the superset it belongs to, to understand all possible configurations of this set. In light of this and in light of the previous geometric treatment, suppose a spherical satellite was put in the GEO, with a fixed attitude with respect to earth. To an equatorial observer directly below the satellite,

the satellite will go through a whole phase throughout the night, similar to the lunar cycle, but it spans only 12 hours. The plane perpendicular to the solar rays, will touch a single point on the spherical object moving from -90˚ to +90˚ in 12 hours. Since the object's attitude is fixed, the solar cycle contributes only 23.5˚ of variation per solstice. This restricts our observations to a $180° \times 67°$ wedge of photometric observations, not counting day-time observations.
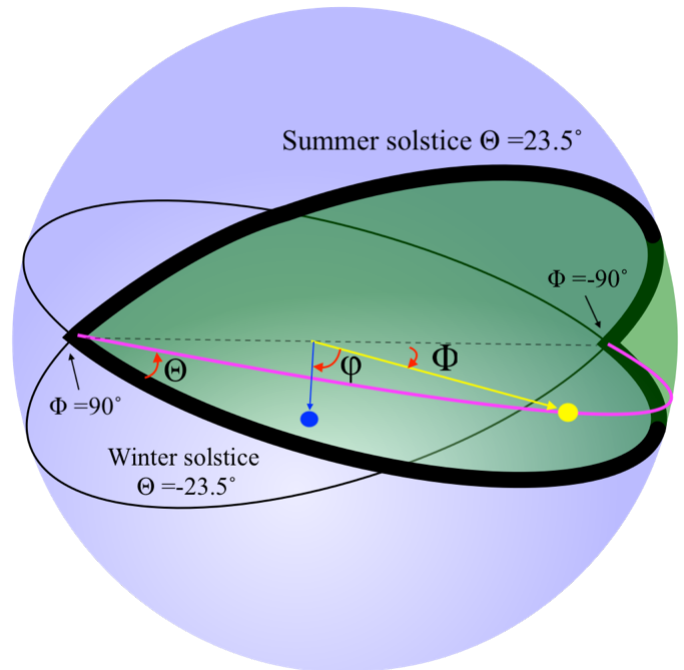

Figure 13. An illustration showing the coordinates of accessible photometric observation in green. The pink arc represents a single light-curve observation.

Figure 13 illustrates the wedge of accessible photometric observations in green, with the pink line as an example of a single light-curve observation. For accuracy, there should be a small purple circle of inaccessible area in the middle of the green wedge for when the earth's shadow eclipses satellite. By sampling this space over the course of 6 months (between the solstices) a light-plane can be constructed, which for a smooth sphere will result in

constant brightness along Θ, and a gradient along Φ with a maximum at $\Phi = 0$.

Building on this model, one can add granularity to this sphere which will impart its signature on our light-plane, for example by placing a small reflective circle on a diffusive sphere, its diameter can be calculated with a single light-curve passing through its middle.

Notably, the light-plane observed changes from observer to observer depending on where on earth they are located, in fact any movements along the latitudinal or longitudinal direction changes the whole space of accessible curves, so light-curves taken of an irregularly shaped GEO object at a location on earth are not reproducible elsewhere.

Since the satellite's attitude is fixed with respect to the earth, for a static earth observer, a single year of measurements is sufficient to sample the whole accessible light-plane, the constructed light-plane that such an observer has recorded, varies smoothly as the observer moves along Θ or Φ, thus each earth bound (Θ, Φ) coordinate maps to a $67° \times 360°$ light-plane, since observations along Φ is not restricted to $\pm 90°$.

Importantly the plane perpendicular to the sun rays, shown by the yellow dot in figure 13, is moving at the (constant) sidereal rate along Φ, which is different from the (non-constant) rate of change of φ, and φ can be found by calculating the angular difference between the sun vector (yellow) and the observer vector (blue).

C. The Astra light-curves

In light of this, our light curve data in figure 8 represents 5 passes through the available light-plane, with an angular difference of $\Theta = 67°/365$ days $= 0.18°$ each night.

Broadcasting satellites such as the ones under study are 3-axis stabilized with very high precision, thus it is fair to assume that the observer vector in this satellite-earth coordinate system is fixed over time, this is what causes the continuity in the data from night to night.
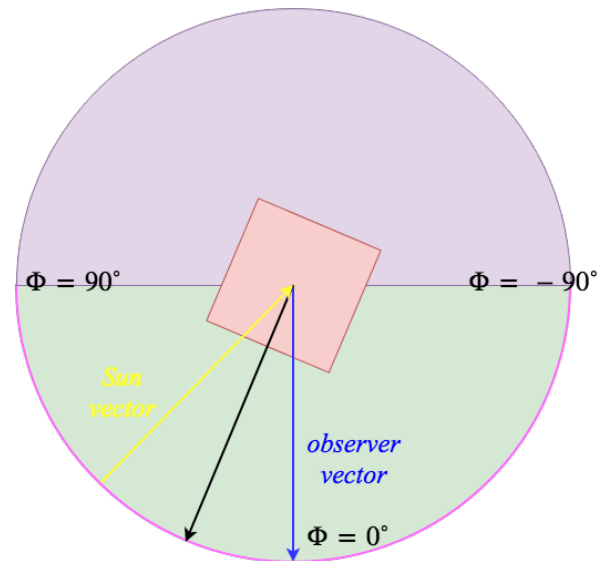

Figure 14. Showing the light-curve slice from figure 13. By construction, the observer vector is fixed at $\Phi = 0$, and the sun vector is circling the satellite at a rate of $15°$ per hour. Considering a box satellite design, the angular difference between the observer vector and the attitude vector can be calculated by observing the maximum in brightness.

Despite the limited sample size, by making a few assumptions about the size and shape of the satellites it is possible to infer a few physical details. The location of maximum brightness in three of the satellites does not correspond to minimum phase angle, this can be explained by considering a 3 axis stabilized box satellite. In such a satellite design, the

moment of highest reflectivity will depend on the attitude of the satellite along Φ and the location of the observer along Φ. By construction, the minimum phase angle corresponds with the observer and sun vector at $\Phi = 0$. The left side of figure 12 shows that the glint in the 1KR curve corresponds with minimum φ, figure 12 (right) shows this to be at 22:33. Knowing this allows us to use the right side of figure 12 to read off the separation along Φ between the observer vector and the attitude vector, this angle is $2d\Phi = 40 \min = 10°$, see figure 14 for an illustration of this. From our previous calculations we found that an angular distance of 5° with respect to the satellite corresponds to approximately 28° of separation along the earth's surface. Incidentally the longitudinal difference between our telescope in La Palma and the middle of the coverage zone shown in figure 15, near west of Germany is about 28°.
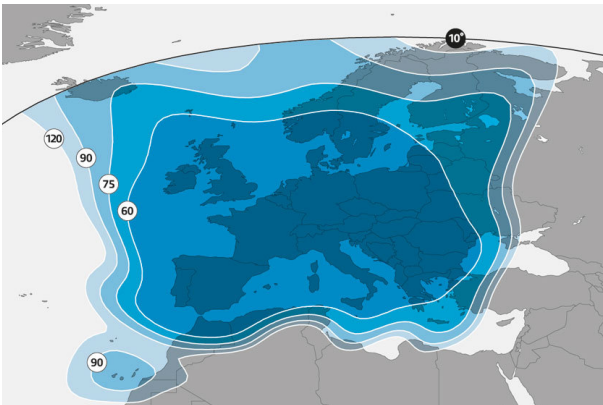

Figure 15. Coverage area of the Astra 1KR satellite published by the SES. The longitudinal difference between the telescope in La Palma (located near the 90 circle) and the middle of the dark blue zone west of Germany is about 28°.

Further building on the cube satellite model, we see that the Astra 1KR reaches minimum brightness at 90°, which is what is expected

from a 3 axis stabilized cuboid, 3D illustrations of the Astra 1KR polished by satellite operators reflects this design, see figure 16.

Figure 16. illustration of the Astra 1KR published by SES.

Finally, the prominent double peaks shown in the 1M and 1L curves illustrates the distorting effect of plotting light-curves as a function of phase angle, because the rate of change of the phase angle is not constant, the phase difference between the two peaks is 3.5° for 1M and 7° for 1L. When compared in the time dependent figure 9 (right), they both correspond with 30 minutes or 7.5 ° along Φ. The cause of these features is not clear, but by making some admittedly large assumptions, it is possible to arrive at a length value of an instrument on the surface of the satellite. Coming back to the spherical model built up in section III.B, assuming a radius of 2.5 m, and an instrument on its surface characterized by two edges of high reflectivity, an angular difference of 7.5° corresponds with an arc length of 0.3 m.

Many more interesting features can be seen in the curves, but with a sample size of essentially

16

1, due to the close proximity of the curves, it is difficult to draw conclusion.

V. CONCLUSION

The process of constructing light-curves from CCD images of geostationary satellites was demonstrated in this text. This project involves the merging of two related yet distinct disciplines, *CCD astronomy*, encompassing the bulk of the data acquisition process, secondly the analysis and interpretation of the data, involves applying principles of astrodynamics and orbital mechanics.

The aim of this project was to a understand how certain physical dynamics of objects in the GEO relate to the observed photometric features uncovered by our CCD surveys. To this end, a model was developed revealing the data to be essentially two dimensional. By making a few assumptions about the shape of the satellites, one of the components of the angle between the satellite's attitude and the observer was estimated to be around 5˚, this is reflected in the broadcasting coverage map provided by the satellite's operators. With expert knowledge in satellite design, potentially more features in the curves can be interpreted.

Astronomical light-curve observations, has conditioned us to think of photometric measurements as a process of sampling a fundamentally one dimensional signal source. This investigation into the light-curves of geostationary objects, suggests a more appropriate two dimensional construction of photometric observations, i.e. light-planes. By constructing a light-plane as proposed in section III.B, variations along Φ and Θ can be examined and not just along Φ, as is the case with light-curves. Thereby, even variations along the diagonal of a 3-axis stabilized satellite can be measured. This model however, is not constricted to GEO observation, but can be generalized to non-GEO orbiting objects and even objects rotating about their axis, at a not inconsiderable conceptual and computational cost.

REFERENCES

[1] C. Collis, The geostationary orbit: a critical legal geography of space's most valuable real estate, The Sociological Review 57(1_suppl) (2009) 47-65.

[2] S. Gorove, The geostationary orbit: issues of law and policy, American Journal of International Law 73(3) (1979) 444-461.

[3] R. Choc, R. Jehn, Classification of geosynchronous objects, European Space Operations Centre, European Space Agency (22) (2018).

[4] C. Henry, ExoAnalytic video shows Telkom-1 satellite erupting debris, (2017).

[5] D.A. Vallado, Fundamentals of astrodynamics and applications, Springer Science & Business Media2001.

[6] J.J. Pocha, An Introduction to Mission Design for Geostationary Satellites, Springer Science & Business Media2012.

[7] C. Levit, W. Marshall, Improved orbit predictions using two-line elements, Advances in Space Research 47(7) (2011) 1107-1115.

[8] E.S.O. Centre, ESA's Annual Space Environment Report, (Issue 2 Rev 0) (2018).

[9] I.-A.S.D.C. Committee, IADC space debris mitigation guidelines, IADC-02-01 Revision 1 (2007).

[10] P. Seitzer, E. Barker, B. Buckalew, A. Burkhardt, H. Cowardin, J. Frith, C. Kaleida, S.M. Lederer, C.H. Lee, The small size debris population at GEO from optical observations, (2017).

[11] B.W. Carroll, D.A. Ostlie, An introduction to modern astrophysics, Cambridge University Press2017.

[12] G.F. Knoll, Radiation detection and measurement, 3rd ed., J. Wiley, New York, 2000.

[13] W. Gressler, J. DeVries, E. Hileman, D. Neill, J. Sebag, O. Wiecha, J. Andrew, P. Lotz, W. Schoening, LSST Telescope and site status, Ground-based and Airborne Telescopes V, International Society for Optics and Photonics, 2014, p. 91451A.

[14] W. Romanishin, An Introduction to Astronomical Photometry Using CCDs, University of Oklahoma 17 (2006).

[15] S.B. Howell, Handbook of CCD astronomy, Cambridge University Press2006.

[16] D. Lang, D.W. Hogg, K. Mierle, M. Blanton, S. Roweis, Astrometry. net: Blind astrometric calibration of arbitrary astronomical images, The astronomical journal 139(5) (2010) 1782.

[17] C. Früh, T. Schildknecht, Accuracy of two-line-element data for geostationary and high-eccentricity orbits, Journal of guidance, control, and dynamics 35(5) (2012) 1483-1491.

[18] K. Mighell, CCD aperture photometry, Precision CCD Photometry, 1999, p. 50.

[19] E. Bertin, S. Arnouts, SExtractor: Software for source extraction, Astronomy and Astrophysics Supplement Series 117(2) (1996) 393-404.

[20] E. Rybka, The zero-point in stellar photometry, Vistas in Astronomy 2 (1956) 1111-1115.

[21] A.G. Brown, A. Vallenari, T. Prusti, J. De Bruijne, F. Mignard, R. Drimmel, C. Babusiaux, C. Bailer-Jones, U. Bastian, M. Biermann, Gaia Data Release 1-Summary of the astrometric, photometric, and survey properties, Astronomy & Astrophysics 595 (2016) A2.